Journal of Energy Storage 76 (2024) 109737

Contents lists available at ScienceDirect

Journal of Energy Storage

journal homepage: www.elsevier.com/locate/est

Research papers

Revealing bimetallic synergy in van der Waals $AgInP_2Se_6$ nanosheets for alkali metal ion battery electrodes

Yan-Jie Liao, Yi-Yen Hsieh, Yi-Chun Yang, Hsing-Yu Tuan *

Department of Chemical Engineering, National Tsing Hua University, Hsinchu 30013, Taiwan

ARTICLE INFO

Keywords:
Alkali metal ion batteries
Metal trichalcogenides
Anode
Bimetallic
Two-dimensional

ABSTRACT

We report two-dimensional $AgInP_2Se_6$ (AIPSe) bimetallic phosphorus trichalcogenides nanosheets as anodes for advanced alkali metal ion batteries (AMIBs). The intrinsic layered architecture of this compound not only facilitates rapid charge propagation but also accentuates ion storage due to its expansive surface area. The integration of the bimetallic component results in a synergistic enhancement in electronic/ionic conductivity and optimizes the redox dynamics of multi-electronic materials, eventually attaining superior electrochemical characteristics. Moreover, the accompanying deposition of metallic silver during electrochemical processes reduces battery polarization, while the presence of metallic indium acts as an efficacious structural stabilizer, effectively inhibit dendrite proliferation. As an anode electrode coupled with graphite (G) in lithium-ion (LIBs) and potassium-ion batteries (PIBs), AIPSe@G anodes for LIBs achieve 707.8 mA h g^{-1} at 0.1 A g^{-1}, retain over 900 cycles at 2.0 A g^{-1}, and demonstrate 318.5 mA h g^{-1} at 3.0 A g^{-1} rate capability. For PIBs, they reach 480.3 mA h g^{-1} at 25.0 mA g^{-1}, sustains for 550 cycles at 250 mAg^{-1}, and offers 214.2 mA h g^{-1} at 3.0 A g^{-1} rate performance. Comprehensive full cell tests further endure 100 cycles in both LIBs and PIBs under diverse current regimes. Our study pioneers a new direction for AMIB anode materials, emphasizing the advantages of integrating bimetallic features into two-dimensional frameworks to boost electrode dynamics and achieve consistent conversion reactions.

1. Introduction

Given their high energy density, long cycle life, minimal environmental impact, and easy maintenance, alkali metal ion batteries (AMIB)—such as lithium-ion (LIBs), sodium-ion (SIBs), and potassium-ion (PIBs)—are essential for energy storage [1–5]. They're suited for a variety of uses, from handheld electronics to electric vehicles [6–10]. AMIB anode materials are classified by their reaction behavior into intercalation compounds [11], carbonaceous materials [12,13], alloy materials [14–16], and conversion materials [17,18]. Conversion-type anodes for AMIB electrodes offer higher specific capacity than commonly used carbon-based materials (only ~370 mA h g^{-1} for Li, ~279 mA h g^{-1} for K), making them promising for AMIBs [19,20]. Conversion electrodes chemically form new compounds during charge storage, but suffer from low conductivity and significant volume expansion, with metal halide cathodes expanding 50–100 vol% and conversion anodes 150–450 vol%. To enhance stability and performance, current solutions include carbon composites, structural optimization of active materials, better electrolytes, and doping for improved ion/electron transport [21,22].

Two-dimensional materials, atomically thin and bonded by covalent or ionic forces, layer via van der Waals interactions [23]. Their 2D nature enhances alkali ion diffusion, electron transfer, and ion intercalation while evenly distributing stress during ion insertion [17]. Stress management in 2D materials prevents electrode breakdown, enhancing electrochemical performance and AMIB's long-term cycling [24]. Their large surface area ensures uniform charge distribution due to increased electrolyte contact, while exposed atomic sites boost ion adsorption and anode capacity [25]. This structure allows for shorter ion path distances, even stress distribution during ion insertion/extraction, prevention of electrode pulverization, and offers many active sites for ion storage due to its large surface area [26]. 2D materials like graphene [27–29], hexagonal boron nitride [30–35], transition metal dichalcogenides (TMDs) [36–43], and transition metal phosphorus trichalcogenide (MPTCs) [44–46] are studied extensively. Thinius et al. identified the key role of interlayer interactions, like van der Waals forces, in the stability of graphite and LiC_6 [47]. Xie et al. created vertically aligned MoS_2 nanosheets for rapid electron transport [48]. Zhou et al. report

* Corresponding author.
E-mail address: hytuan@che.nthu.edu.tw (H.-Y. Tuan).

https://doi.org/10.1016/j.est.2023.109737
Received 5 September 2023; Received in revised form 9 November 2023; Accepted 13 November 2023
Available online 23 November 2023

VS_2's layered structure, which promotes alkali metal ion intercalation due to high adsorption energy and low diffusion barriers, showing its significant potential for electrochemical storage [49]. However, 2D materials faces challenges like significant volume changes between layers, causing irreversible capacitance decay [50]. Xie et al. discovered enhanced cycle performance in ReS_2 alkali metal ion electrodes due to conversion reactions [51]. Contrary to this, the $K_{0.8}Ti_{1.73}Li_{0.27}O_4$@rGO presented by Hou et al., while exhibiting consistent cycle performance as a general-purpose anode, demonstrates a restricted reversible capacity [52]. Thus, developing 2D anodes with both high reversible capacity and long-lasting cycle performance is crucial.

MPTCs offer potential as future energy storage materials due to Mott-Schottky heterointerfaces and swift electron/ion transfer [53]. These can be either monometallic ($M^{II}PX_3$) or bimetallic ($M^{I}_{0.5}M^{III}_{0.5}PX_3$), where M^{II} includes divalent cations like V, Mn, and others; M^{I} covers monovalent cations such as Ag or Cu; M^{III} encompasses trivalent cations like Cr, V, and more; and X represents S or Se [54]. Bimetals generally have better conductivity than single metals [55]. Introducing diverse divalent metals to MPTC can polarize bonds in the bimetallic system due to varying electronegativities, influencing charge transport [56]. Zhong et al. introduced a bimetallic thiophosphate alloy $Zn_xCo_{1-x}PS_3$ and CoS_2 as a 2D/3D heterostructure for lithium storage. Their calculations indicated that zinc atoms likely replace Co atoms in $CoPS_3$, altering the electronic structure and creating an asymmetric electric field. ZCPS-Y has a lower lithium intercalation energy than $CoPS_3$, suggesting easier lithiation after zinc alloying. The wide planes inherent to $Zn_{0.5}Co_{0.5}PS_3$ furnish numerous anchoring points for CoS_2, thereby elevating the electrochemical efficiency of its 2D/3D heterostructure [57]. However, the benefits of bimetallic MPTCs as AMIB anodes are yet to be defined in practical applications.

In our study, we introduce 2D bimetallic MPTCs as anode materials for AMIBs. These 2D materials distribute ion-induced stress, preventing electrode damage. Incorporating bimetals, specifically silver and indium, elevates electrochemical performance by enhancing electron/ion conductivity and cycle stability. Silver within these compounds prevents nanosheet aggregation, enhancing the material's structural stability and overall durability. Indium, with its electrochemical inertness, serves as a buffer against volume expansion in redox reactions. When paired with graphite structures that provide both shielding and mechanical support, the performance of the 2D materials is significantly improved. In the electrochemical test, the LIBs with AIPSe@G as the anode electrode has a cycle stability of 900 cycles and a capacity decay of 0.021 % per cycle (with a maximum capacity of 579.9 mA h g^{-1} at 2.0 A g^{-1}). The PIB's cycle stability reaches 550 cycles, with a capacity decay of 0.085 % per cycle and a maximum capacity of 397.2 mA h g^{-1} at 0.25 A g^{-1}. These findings reveal the potential of 2D bimetallic MPTC as a versatile anode material for AMIBs (Scheme 1).

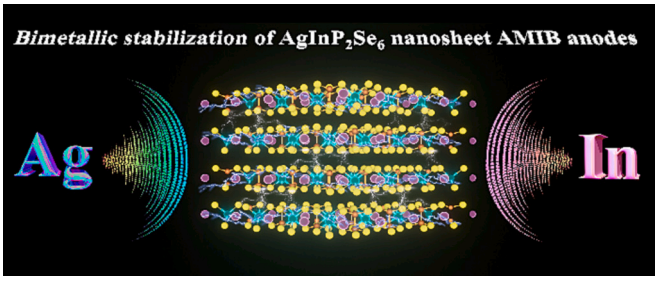

Scheme 1. A two-dimensional AIPSe bimetallic nanosheet. Silver interacts closely with intermediates, stabilizing the metal chalcogenide structure, while indium provides electrochemical stability, buffering volume expansion in redox reactions and reducing dendrite formation.

2. Results and discussion

To elucidate the distinctions between InSe and AIPSe, density functional theory (DFT) calculations were conducted. As depicted in Fig. 1a and b, the electronic band structures of the respective materials are presented. While InSe exhibits electrical conductivity, AIPSe appears as an indirect bandgap semiconductor, characterized by a constricted bandgap of 0.289 eV. We also examined the total density of states (TDOS) for InSe and AIPSe (Fig. 1c, d). InSe shows continuous states near the Fermi level (Fig. 1c inset), confirming its conductivity. In contrast, AIPSe displays a discontinuity near the level (Fig. 1d inset), corresponding to the electronic band structure in Fig. 1b. The PDOS in Fig. 1d reveals that states near the valence band maximum (VBM) primarily originate from the p-orbital of Se atoms and d-orbitals of Ag atoms, whereas states near the conduction band minimum (CBM) come from the p-orbitals of Se atoms. Liao et al. noted that a broader surface d-band can elevate states' energies, resulting in stronger adsorption bonding and suppressing the chalcogenide shuttle effect common in negative electrodes [58]. Through Bader analysis (Fig. 1e, f), we found that in the InSe unit cell, the In atom lost 0.57 electrons while the Se atom gained the same amount. In the AIPSe unit cell, P, Ag, and In atoms lost 0.40, 0.28, and 0.95 electrons respectively, with Se atoms gaining 0.34 electrons. All electrons shed by P, Ag, and In were transferred to Se atoms. The simulation conducted by Zhang et al. indicates electron accumulation around Se atoms and depletion around Ag and In atoms, a finding consistent with our Bader charge transfer analysis [59]. Fig. 1g and h displays the 3D charge density difference diagrams for InSe and AIPSe. These diagrams, where yellow indicates electron accumulation and blue denotes depletion, reveal that AIPSe has superior electron transport compared to InSe. Compared to InSe, adding Ag to AIPSe leads to greater charge transfer in In (red box), as confirmed by Bader analysis. Additionally, AIPSe concentrates more charges on Se near atoms (purple box) than InSe does. Simulation results indicate AIPSe has superior charge transport ability to InSe.

Pure elements Ag, In, P, and Se, combined in a 1:1:2:6 ratio, were sealed in a vacuum tube and heated at 750 °C for 24 h, producing the layered compound AIPSe. This compound, with a hexagonal P-31c space group (PDF 00–048-0819), has lattice parameters a = b = 6.483 Å, c = 13.33 Å, angles α = β = 90°, γ = 120°, and a unit cell volume of 485.19 $Å^3$. AIPSe's layers are bonded by van der Waals forces and its composition verified by ICP-OES, SEM-EDS and TEM-EDS results. (Figs. S1–3 and Table S1) An AIPSe@G composite was produced by ball milling AIPSe at 200 rpm for 24 h, exfoliating it into atomically thin, crystalline nanosheets by overcoming van der Waals forces. Adding graphite to AIPSe layers formed a composite addressing AIPSe's volumetric changes, potentially boosting synergy and enhancing alkali metal ion storage performance. Fig. 2(a) and (b) shows atomic force microscopy (AFM) measurements that illustrate a uniform distribution of flake-like AIPSe on the substrate. A single flake has an approximate thickness of 12 nm. As depicted in Fig. 2(c) and (f), Scanning electron microscopy (SEM) and transmission electron microscopy (TEM) analyses show AIPSe's flake-like morphology with lateral dimensions nearing 500 nm. The single-crystal structure of AIPSe is confirmed by SAED in Fig. 2d. HRTEM shows a lattice fringe spacing of 0.286 nm, matching AIPSe's (1 0 4) plane, as seen in Fig. 2e. STEM-EDS mapping in Fig. 2g illustrates a consistent elemental distribution in AIPSe, while TGA estimates the carbon content of the AIPSe@G composite at approximately 22 %. (Supporting information Fig. S4).

Fig. 3a shows the XRD patterns for AIPSe, AIPSe@G, and InSe. Diffraction peaks at 13.27°, 38.7°, 48.6°, and 58.55° correspond to the (0 0 2), (1 1 4), (3 0 0), and (2 2 2) planes. Both AIPSe and AIPSe@G peaks match well with $AgInP_2Se_6$ (PDF 00-048-0819), indicating the product's high purity. Similarly, the diffraction peaks of InSe are in line with the InSe phase (PDF 04-003-2450), appearing at 10.6°, 21.3°, and 45.2°, which correspond to the (0 0 3), (0 0 6), and (1 1 0) planes. These patterns suggest a rhombohedral structure with a space group of R-3 m.

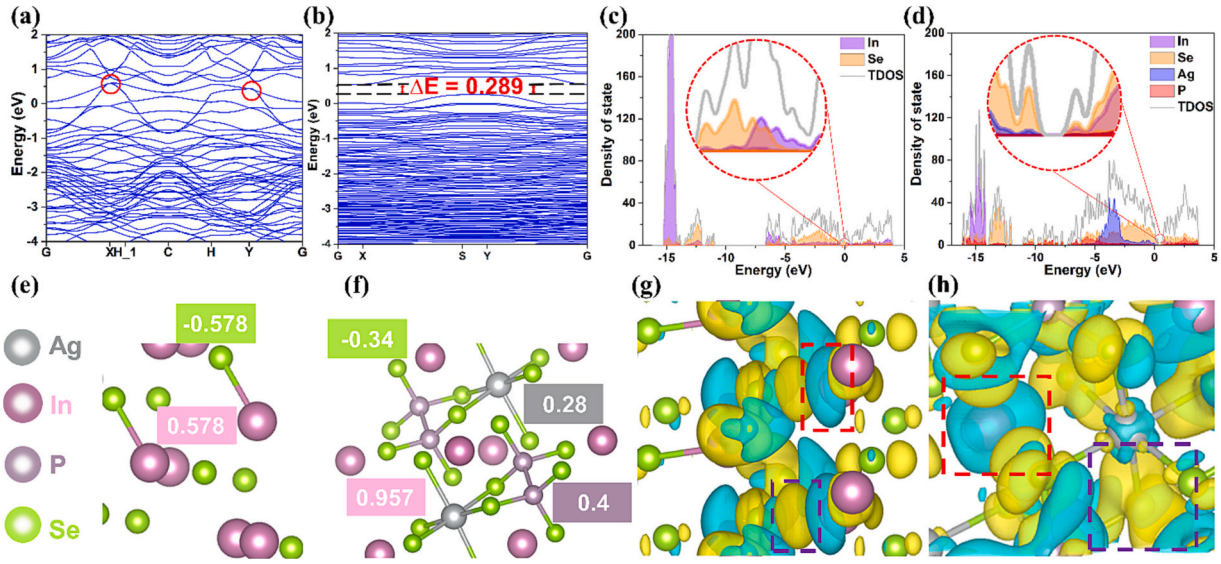

Fig. 1. Band structure of (a) InSe, (b) AIPSe. Calculated DOS of (c) InSe, (d) AIPSe. Bader charge of the atoms at the active sites of (e) InSe, (f) AIPSe. Calculated 3D charge density difference (CDD) of (g) InSe, (h) AIPSe.

The determined lattice parameters are a = b = 4.005 Å, c = 24.96 Å, with α = β = 90°, γ = 120°, and a unit cell volume of 346.65 Å^3. As shown in Fig. 2b, the Raman spectra of AIPSe and AIPSe@G reveal the presence of carbonaceous components, with peaks at 1340 cm^{-1} (D band) and 1580 cm^{-1} (G band). These bands provide insights into the disordered and graphite carbon in the structure, exhibiting an intensity ratio (I_D/I_G) of 0.74. Such peaks indicate the quantity of structural defects and the level of graphitization, with an increase in defects potentially enhancing the adsorption and insertion capabilities of K^+ [24]. The surface chemical composition and electron state of AIPSe were analyzed using X-ray photoelectron spectroscopy (XPS), as shown in Fig. 2c to e. Specifically, the Ag 3d spectrum can be deconvoluted into two peaks located at 368.4 eV and 374.4 eV, corresponding to Ag $3d_{5/2}$ and Ag $3d_{3/2}$ bands, respectively [60]. Peaks at 445.1 eV and 452.8 eV in the high-resolution In 3d spectrum are assignable to In $3d_{5/2}$ and In $3d_{3/2}$. The P 2p spectrum shows peaks at 132 eV and 133.2 eV that correspond to P $2p_{3/2}$ and P $2p_{1/2}$. A notable peak at a higher binding energy (134.5 eV) is attributable to PO_x, stemming from surface oxidation [24]. The peak at 138.1 eV can be attributed to the Se LMM peak [61–63]. Finally, the high-resolution Se 3d spectrum exhibits peaks at 55.4 and 56.5 eV, matching Se $3d_{5/2}$ and Se $3d_{3/2}$, respectively. An additional peak at 139 eV is likely due to the overlap of the Se Kα line and P 2p core levels [17].

In evaluating the electrochemical capabilities of the AIPSe@G electrode for lithium-ion storage, Fig. 4a presents the initial five CV cycles (0.01–3.0 V at 0.2 mV/s). The initial cycle shows a cathode peak around 1.51 V, indicating the electrolyte decomposition and the SEI film [64]. Later cycles present two additional peaks, indicating lithium-ion insertion into AIPSe, forming Ag, InLi, Li_3P, and Li_2Se. The subsequent anode process peak implies the delithiation of InLi, Li_3P, and Li_2Se, yielding InSe, Se, and amorphous P. Peak overlaps from the second CV cycle suggest strong reversible electrochemical performance. Fig. 4b displays the initial three GCD cycles at a current density of 200 mA g^{-1} with an initial charge/discharge capacity of 815/682.3 mA h g^{-1} and a Coulombic efficiency of 83.7 %. The irreversible capacity is attributed to the formation of SEI film and other irreversible reactions. Fig. 4c shows the rate performance of AIPSe@G electrode specific capacities from 577.8 to 318.5 mA h g^{-1} over current densities of 0.025 to 3.0 A g^{-1}. Notably, capacity nearly returns to initial level after reducing current density, pointing out high electrode reversibility at increased rates. Fig. 4d and e compares the cycling and long-cycling performances of AIPSe@G and InSe@G electrodes, with AIPSe@G outperforming InSe@G in cycling performance. Motivated by the impressive long-cycle performance of AIPSe@G in lithium-ion half cells, we extended our investigation to assess its potential as an anode in potassium-ion half cells. Fig. 4f exhibits the first five CV cycles of the AIPSe@G electrode for PIBs, differing from Fig. 4a. The reason is the conversion reaction of AIPSe form the different intermediate products after Li^+ and K^+ intercalation/extraction. In this case, the first cycle shows a cathodic peak at roughly 0.86 V due to the electrolyte decomposition and the formation of SEI film [64], and another at 0.43 V for Ag, In, K_4P_3, and K_2Se formation. The anodic process exhibits a peak at 1.97 V, corresponding to the depotassiation of Ag, In, K_4P_3, and K_2Se to form AIPSe. Fig. 4g presents the initial three GCD cycles at 25 mA g^{-1} current density, with the first charge/discharge capacity found at 673.6/436.5 mA h g^{-1}. The lower initial Coulombic efficiency of 64.8 %, compared to LIBs, could be attributed to the smaller ionic radius of Li^+ allowing for a higher quantity of ions. Fig. 4h presents the rate performance of the AIPSe@G electrode in PIBs, with specific capacities ranging from 455.3 to 214.2 mA h g^{-1} across 0.025 to 3.0 A g^{-1} current densities, again illustrating the impact of the alkali metal's ionic radius on capacity. Fig. 4i summaries the cycling performance, revealing a discharge capacity of 411.4 mA h g^{-1} after 40 cycles. Even after 550 cycles at 0.25 A g^{-1}, the AIPSe@G electrode retains a high reversible capacity of 210.6 mA h g^{-1}.

The differences in electrochemical performance have limited the use of the AIPSe electrode in all types of AMIBs. The underlying factors contributing to these performance differences between LIBs and PIBs, despite both employing the same type of electrode, have been the subject of extensive investigation. It's widely understood that the larger radius of the K^+ leading to slower diffusion kinetics contributes to the poorer performance of PIBs [24]. Additionally, this reason also may be the different intermediate products after intercalation/deintercalation of Li^+ and K^+. Among them, P reacts with Li+ and K^+ to form Li_3P and K_4P_3, respectively. The volume expansion of K_4P_3 (411.78 %) is significantly higher than that of Li_3P (277 %) [65,66]. Large volume expansion leads to sluggish reaction kinetics and poor electrochemical reversibility. To investigate the reasons behind the varied performance of AIPSe electrodes, we performed a kinetics analysis. This involved conducting a rate-dependent cyclic voltammetry (CV) scan for Li^+ and K^+ on the AIPSe electrode at different scan rates from 0.1 to 1.0 mV/s (Fig. 5a, g), under a temperature of 25 °C. We employed the power law eq. $I = av^b$ for a deeper insight into the AIPSe charge storage mechanism, where 'I' stands for the current, 'v' for the scan rate, and 'a' and 'b' are adjustable constants. The 'b' value in the power equation signifies the

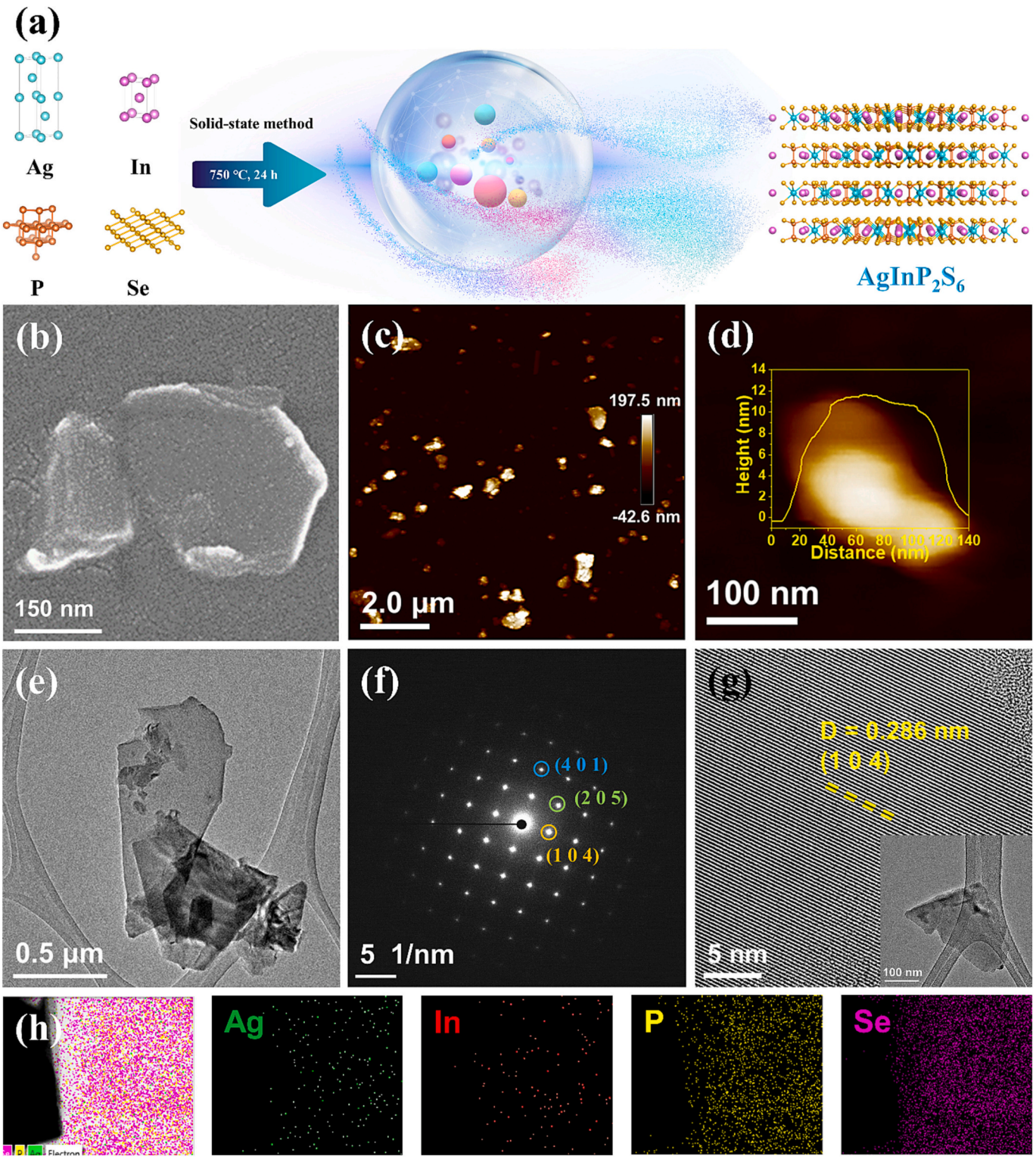

Fig. 2. (a) Schematic illustration of synthesis process of AIPSe, (b) SEM image of AIPSe, (c–d) AFM images of AIPSe, (e) TEM image of AIPSe, (f) SAED pattern of AIPSe, (g) HRTEM of AIPSe. Insets present the single AIPSe flake, (h) EDS mapping images of AIPSe and corresponding elements of Ag, In, P and Se.

prevailing charge storage mechanism, with a value near 0.5 indicating a diffusion-controlled mechanism, and a value close to 1.0 signifying surface-controlled storage [67]. As Fig. 5b and h shows, the 'b' value for the AIPSe@G electrode is approximately 1.0 for LIBs and around 0.8 for PIBs. These findings suggest that surface capacitive behavior is dominant in LIBs, whereas in PIBs, both capacitive and diffusion behaviors play a part in the electrochemical process Fig. 5c and i reveal that the AIPSe@G electrode contributes 87 % and 61 % pseudocapacitive effects for LIBs and PIBs, respectively, at a scan rate of 0.7 mV/s. As scan rates increase (referenced in Fig. 5d and j), the capacitance of PIBs maintains a diminished level. This implies the superior electrochemical kinetics of the AIPSe@G electrode in LIBs and shows the implications of the enlarged K^+ radius on the sluggish kinetics of PIBs. Intermittent Titration Technique (GITT) was used to evaluate the diffusion coefficients of

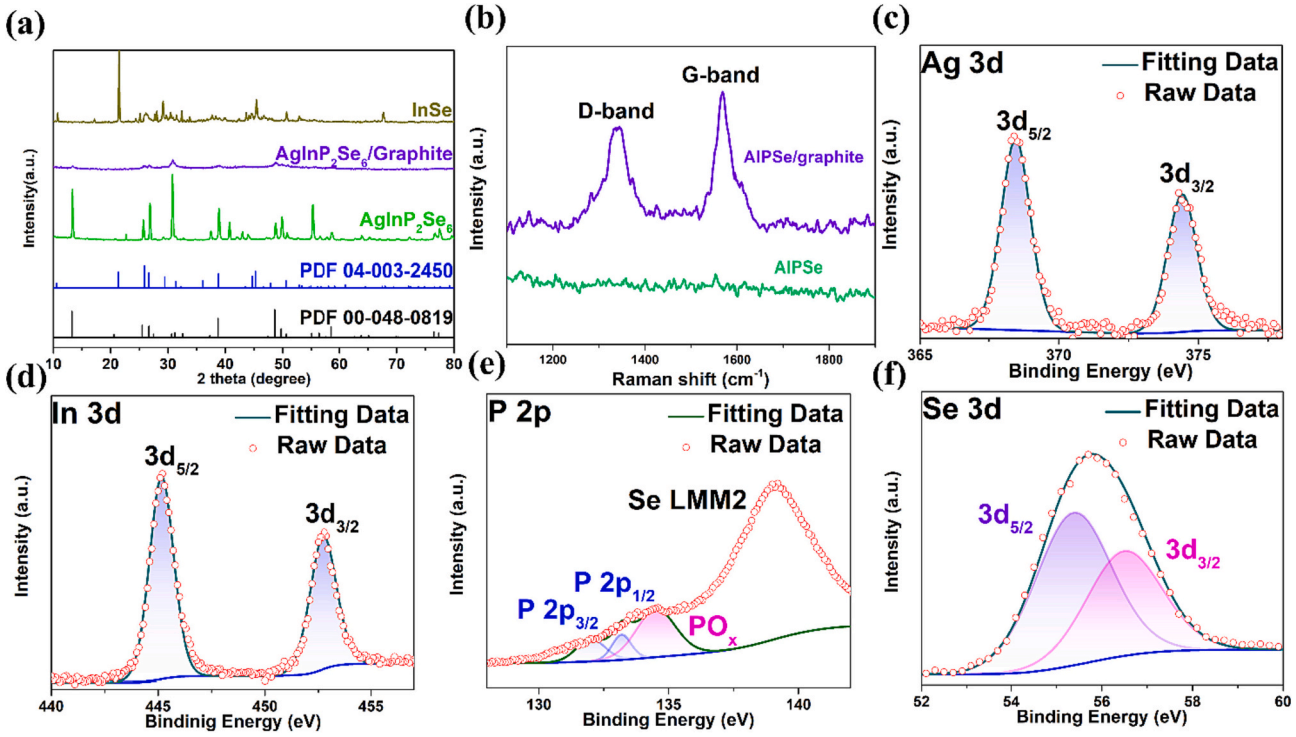

Fig. 3. (a) XRD patterns of bulk AIPSe, AIPSe@G, and InSe. (b) Raman spectra of bulk AIPSe and AIPSe@G. (c–f) High-resolution Ag 3d, In 3d, P 2p, and Se 3d XPS spectra of bulk AIPSe.

LIBs and PIBs in the AIPSe@G electrode, based on the following equation:

$$D_{K^+} = \frac{4}{\pi\tau}\left(\frac{m_B V_M}{M_B S}\right)^2\left(\frac{\Delta E_s}{\Delta E_t}\right)^2 \left(\tau \ll \frac{L^2}{D}\right)$$

where τ denotes the relaxation time; m_B, M_B, and V_M respectively represent the mass, molar mass, and molar volume of the electrode material; S denotes the surface area of the electrode-electrolyte interface; ΔE_s refers to the voltage change triggered by the pulse current; ΔE_t signifies the voltage change during the constant current pulse [68]. Additionally, GITT curves were derived from AIPSe@G electrode during a 20-min charge/discharge at 50 mA g^{-1}, followed by an hour break (Fig. 5e and k). In this process, the diffusion coefficients for Li^+ and K^+ were respectively 7×10^{-11} and 1.3×10^{-11} cm^2 s^{-1}. Furthermore, in-situ EIS was executed (Figs. S5 and S6).

To elucidate the crystallographic transformations in AIPSe during the LIBs charge/discharge cycle, we developed an in-situ XRD battery for real-time structural tracking, supplemented with ex-situ TEM analysis. Figs. 6a and S7 display the initial in-situ XRD spectrum of AIPSe and the associated GCD curve [69,70]. With progressive Li^+ insertion, AIPSe's peak intensity significantly reduces. When discharged to 1.48 V, the peaks at 36.2°, 25.6°, 39.7°, and 42.5°, corresponding to In (PDF 00–005-0642), Li_2Se (PDF 00-023-0072), Ag (PDF 01-087-0598), and Li_3P (PDF 04-014-7866), respectively. At full discharge to 0.01 V, we observe the new peaks at 37.4°, corresponding to InLi (PDF 01-073-6776). It indicates that there is alloy reaction between In and Li [71]. However, when charged from 0.01 V to 3 V, these peaks disappear, and three distinct peaks surface at 25.7°, 29.8°, and 39.7°. These new peaks, corresponding to InSe (PDF 04-003-2450) and Se (PDF 01-086-2246), indicate that the first charge/discharge cycle's reactions are irreversible. Following the full discharge to 0.01 V (Fig. 6b), the ex-situ HRTEM image of the AIPSe electrode reveals four lattice spacings — 0.200, 0.222, 0.207, and 0.212 nm. The spacings correspond to the (3 1 1), (1 0 2), (1 0 3), and (2 2 0) planes of InLi, Ag, Li_3P, and Li_2Se respectively, as confirmed by the SAED pattern (Fig. 6c). Upon full charge (3.0 V), the irreversible reaction is confirmed by ex-situ HRTEM and SAED images of the AIPSe electrode (Fig. 6d and e). Fig. 6d displays the AIPSe electrode's ex-situ HRTEM image at 3.0 V, revealing lattice spacings of 0.200, 0.343, and 0.207 nm for planes (1 0 3), (1 0 1), and (0 1 2). SAED patterns further identify Ag, InSe, and Se (Fig. 6e). The TEM image at 0.01 V is seen in Fig. 6f, with HRTEM in 6 g mirroring 6b. Fig. 6h, at 3.0 V, presents spacings of 0.224, 0.202, and 0.215 nm for Ag, InSe, and Se on planes (1 0 2), (1 0 10), and (4 1 0) respectively. In an attempt to further probe potential intermediate phases and the intercalation/deintercalation process, we conducted Density Functional Theory (DFT) calculations.

Intercalation-based materials typically exhibit a stable charge-discharge voltage plateau, reflective of the lithiation/delithiation dynamics inherent to battery systems [72]. Upon detailed scrutiny via ex-situ XRD and HRTEM analyses, it is evident that InSe primarily undergoes a reaction with lithium ions, yielding a compound denoted as Li_xInSe, where $0 < x < 1$. This structural framework facilitates subsequent lithiation and delithiation events. As delineated in Fig. 6i, our computed voltage for Li_xInSe within the aforementioned range registers at 2.12 V. This value closely aligns with the cathodic peak observed at 2.05 V, as presented in Fig. 4a. In Fig. 6j, we present the migration energy barriers for both InSe and Ag/InSe. A notable distinction is observed: the diffusion energy barrier for Ag/InSe is significantly lower than that of pure InSe. This suggests that the incorporation of metallic silver enhances the diffusivity of lithium ions, effectively reducing their migration energy barrier [60]. As the in-situ XRD, HRTEM, and SAED do not detect any P element, we hypothesize the formation of amorphous P post lithium removal [24]. The TEM-EDS mapping (Figs. S8 and 9) indicates a uniform distribution of Ag, In, P, and Se. Therefore, the conversion mechanism of AIPSe in LIBs can be summarized as follows:

Discharge process:

$$AgInP_2Se_6 + 18Li^+ + 18e^- \rightarrow 2Li_3P + 6Li_2Se + In + Ag$$

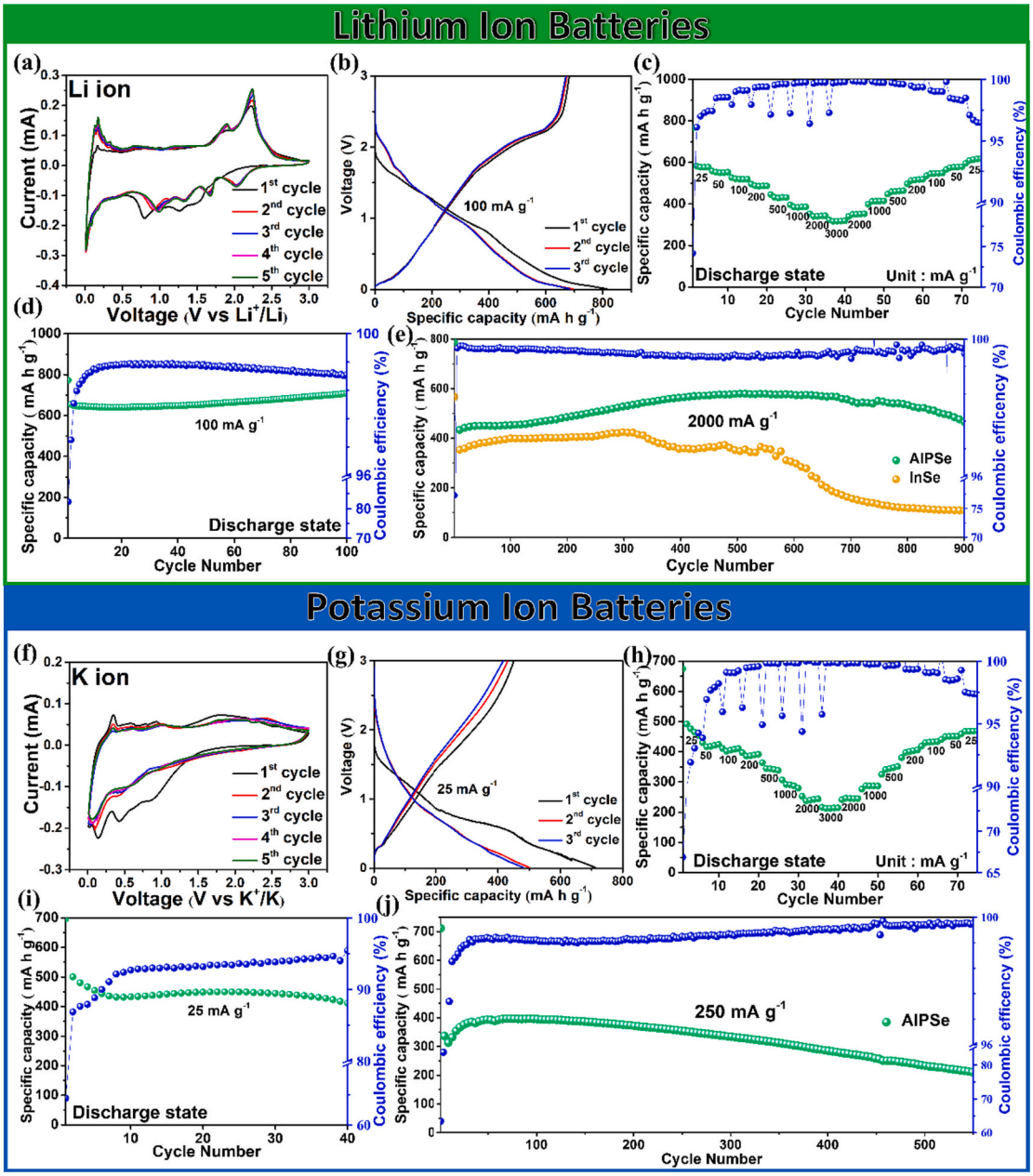

Fig. 4. (a) Voltammetric scans for AlPSe@G in LIBs at 0.2 mV/s sweep rate, and (b) Constant-current discharge-charge plots at a 200 mA g^{-1} current density. (c) Varied current density performance spanning from 0.025 A/g to 3.0 A/g, and cycling durability at (d) 200 mA g^{-1} and (e) 2000 mA g^{-1} for AlPSe@G, as well as InSe@G in LIBs. (f) Voltammetric curves in PIBs for AlPSe@G, acquired at a scan rate of 0.2 mV/s, and (g) Fixed-current discharge-charge plots at 25 mA g^{-1}. (h) Rate capabilities across a spectrum of current densities from 0.025 A/g up to 3.0 A/g, and long-term stability data at (i) 25 mA g^{-1} and (j) 250 mA g^{-1} for AlPSe@G in PIBs.

Charging process:

$$2Li_3P + 6Li_2Se + In + Ag \rightarrow Ag + InSe + 5Se + 6P(amorphous) + 18Li^+ + 18e^-$$

The AlPSe@G electrode surpasses the InSe@G largely due to Ag's close interaction with intermediates during cycling. This interaction stabilizes the metal chalcogenide structure. During delithiation, a bond blocks polyselenides' shuttle effect, improving lithium-ion performance and reaction speed while extending battery life. Li^+ doesn't bond with Ag, reducing volume changes. This boosts Li^+ adsorption, yielding superior capacity and performance. Through DFT calculations, Ho et al. determined that Ag augments the ionic kinetics of metal chalcogenides [60]. CV curves further support this, showing an 88.3 % capacitive contribution at a 1.0 mV/s scan rate — an indication of

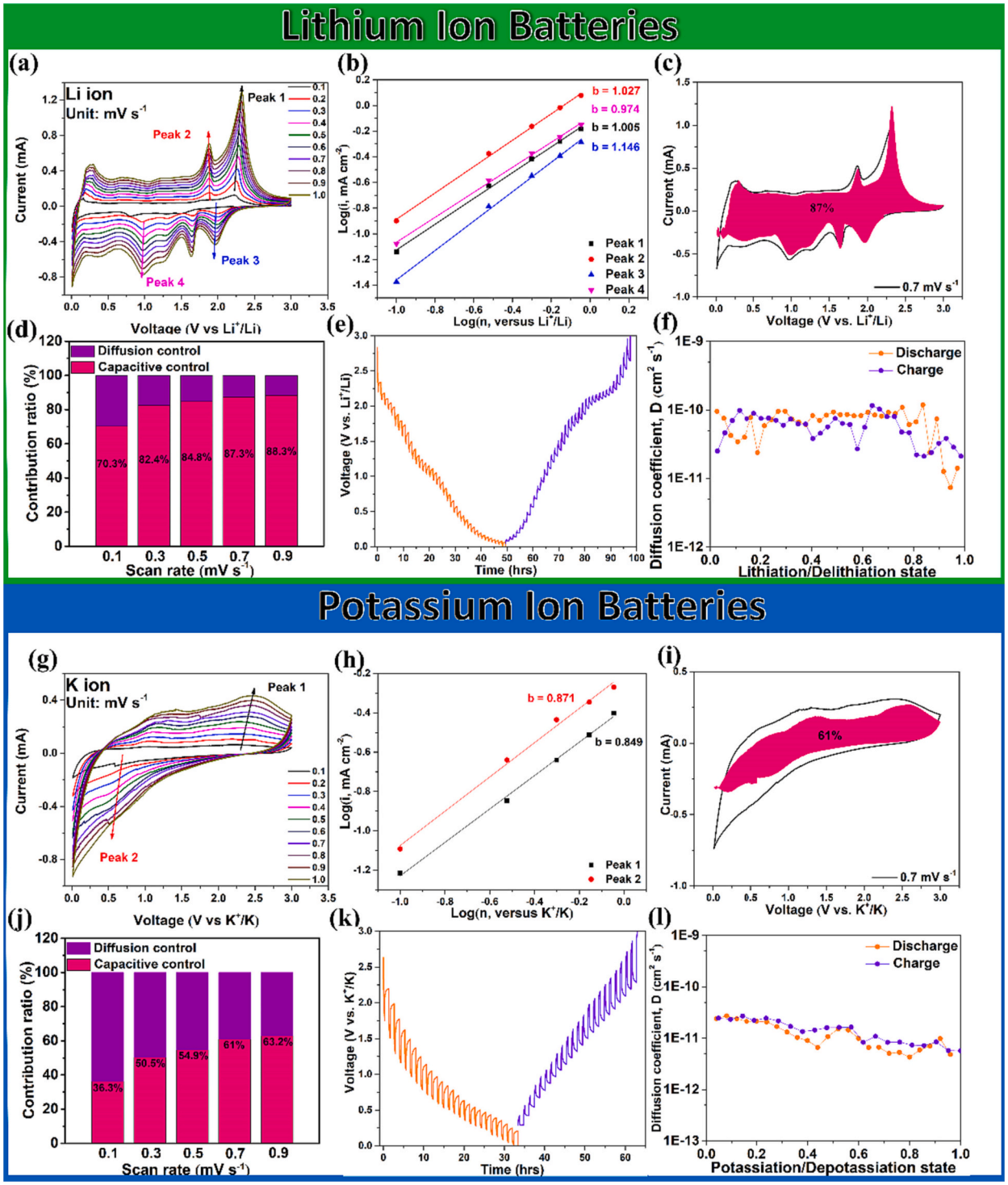

Fig. 5. (a–d) Voltammetric responses for AIPSe@G in LIBs at varying scan speeds from 0.1 to 1.0 mV/s, logarithmic current vs. voltage graphs at particular peaks, capacitance role at a scan rate of 0.7 mV/s, and the proportional contribution of capacitive to diffusion-driven capacities. For AIPSe@G in PIBs, corresponding data is shown in (g-j). Analysis using GITT and the estimated ion diffusion coefficients are presented for LIBs in (e and f) and for PIBs in (k and l).

pseudocapacitive control. Such efficiency stems from Ag's role in enhancing electron/ion migration. Furthermore, InSe, a 2D layered metal chalcogenide, exhibits high electron mobility and thermal stability, as noted by Zhang et al. Its design offers efficient Li^+ channels, facilitating straightforward movement that cuts down on the diffusion path and accelerates the Li^+ diffusion rate [73].

The CV curves from the AIPSe@G electrode in LIBs and PIBs show unique Li^+ and K^+ storage reactions. Ex-situ XRD analysis at different voltages reveals the crystal structure of the reaction products. Fig. 7a indicates that the AIPSe phase persists when the electrode discharges from OCV to 0.5 V, implying the initial potassium ion intercalation doesn't trigger a full phase transition. Upon discharge to 0.01 V, new peaks appear at 31°, 32.8°, 38.9°, 40.3°, matching K_4P_3 (PDF 04-007-1643), K_2Se (PDF 00-023-0470), In (PDF 00-005-0642), and Ag (PDF 01-087-0598). When charged to 0.5 V, peaks associated with the AIPSe phase return. At full charge (3.0 V), K_4P_3, Ag and In peaks vanish when

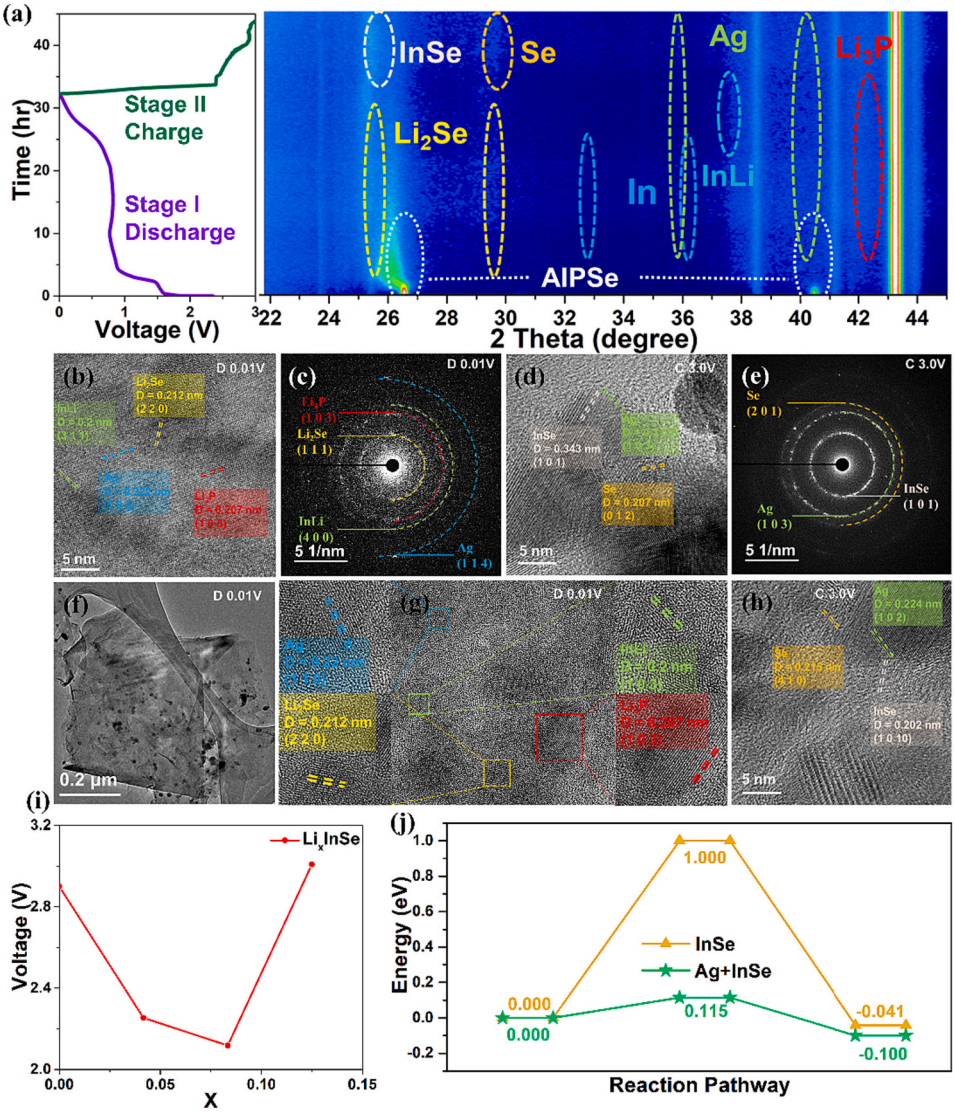

Fig. 6. (a) In-situ XRD patterns captured during AIPSe's inaugural lithiation and delithiation cycles. (b) HRTEM visuals of AIPSe post-discharge to a voltage level of 0.01 V. (c) Electron diffraction patterns captured from AIPSe following its discharge to 0.01 V. (d) High-resolution TEM imagery of AIPSe after being charged up to 3.0 V. (e) Post-charge SAED patterns of AIPSe at 3.0 V. (f) Standard TEM image of AIPSe after it was discharged down to 0.01 V. (g) More high-resolution TEM images of AIPSe following its discharge to 0.01 V. (h) High-resolution TEM views of AIPSe once it has been charged to 3.0 V. (i) Theoretical voltage stages for Li_xInSe phases in relation to varying 'x' values. (j) Comparative analysis of the energy obstacles encountered by Li ions during their diffusion in both Ag + InSe and InSe structures.

AIPSe peaks reappear, indicating a reversible reaction and stable structure, distinct from LIBs. Fig. 7b displays the energy barriers of candidate products. The barrier for AIPSe is 1.33 eV, lower than single metal selenides' 2.26 eV. This indicates bimetallic phosphorus trichalcogenides are more thermodynamically advantageous and also confirms AIPSe remains stable after its first charge-discharge cycle, suggesting the reaction is reversible [74]. To validate the ex-situ XRD findings, Fig. 7c–f displays ex-situ HRTEM and SAED images of the AIPSe electrode at 0.01 V discharge and 3.0 V charge, confirming the K^+ storage mechanism. When discharged to 0.01 V, lattice fringes with spacings of 0.168 nm, 0.224 nm, 0.310 nm, and 0.192 nm are observed, corresponding to the (1 1 2), (1 0 2), (0 2 4), and (4 0 0) planes of Ag, In, K_4P_3, and K_2Se, respectively. (Fig. 7c). The SAED pattern in Fig. 7d shows diffraction rings tied to specific Ag, In, K_2Se, and K_4P_3 planes. After charging to 3 V, AIPSe's lattice fringes, as seen in Fig. 7e, correlate with the (3 0 0) plane and the diffraction rings with AIPSe's (1 1 2) and (2 0 5) planes (Fig. 7f). Fig. 7g shows the HRTEM image discharged to 0.01 V, revealing lattice fringes with spacings of 0.250 nm, 0.247 nm, 0.167 nm, and 0.272 nm, matching the (0 0 4), (0 0 2), (2 4 4), and (2 2 0) planes respectively. Fig. 7h detects AIPSe's lattice fringe with a 0.324 nm spacing corresponding to the (1 1 0) plane. Fig. 7i, charged to 3.0 V, exhibits a sheet-like structure. These observations are consistent with ex-situ XRD results, clarifying the reversible conversion mechanism of the AIPSe@G in PIBs as:

$$3AgInP_2Se_6 + 44K^+ + 44e^- \leftrightarrow 2K_4P_3 + 18K_2Se + 3In + 3Ag$$

The reaction transfers 44 electrons. TEM-EDS images display even distribution of Ag, In, P, and Se (Figs. S10 and 11). Silver precipitation during AIPSe@G electrode charge-discharge highlights active sites, boosting charge transfer, multi-electron reactions, and the composite's electrochemical performance, leading to better cycle stability and less polarization [75]. Within the layered structure, silver strengthens the material, preventing nanosheet aggregation, while the presence of metal indium boosts electron transport due to its conductive properties. Indium also plays a dual role: its electrochemical stability serves as a buffer during volume expansion in redox reactions, and it reinforces interface stability for the electrodes, ensuring long-term cycling [76]. Additionally, indium promotes uniform potassium deposition, curtailing

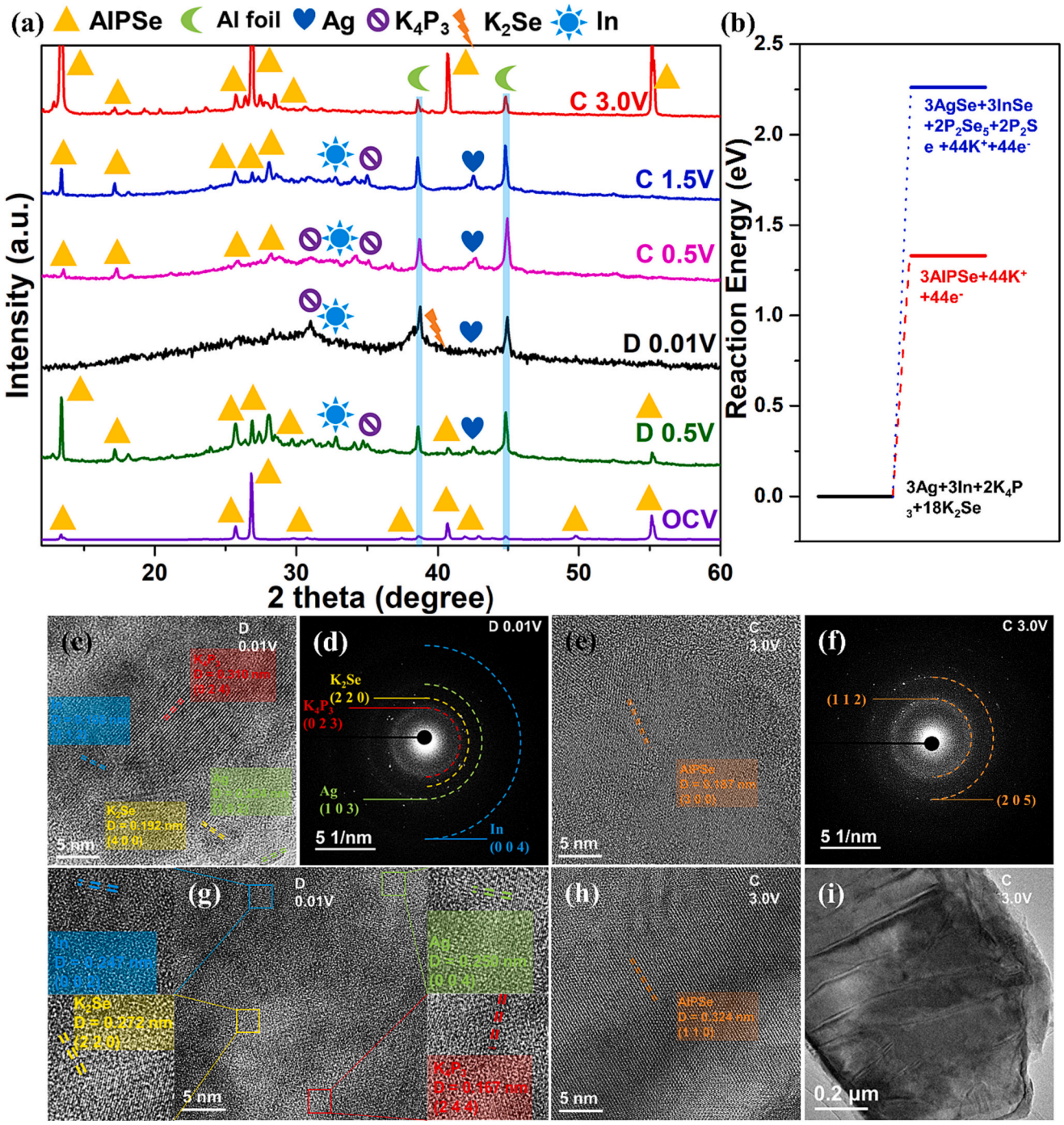

Fig. 7. (a) Ex-situ XRD scans as AlPSe undergoes its potassiation and depotassiation cycles. (b) Computational assessments of reaction energy for potential products during the first charge cycle. (c) HRTEM images of AlPSe once it has been discharged to a 0.01 V voltage level. (d) SAED pattern of AlPSe following its discharge to 0.01 V. (e) HRTEM visuals of AlPSe post-charge to a voltage setting of 3.0 V. (f) SAED patterns of AlPSe subsequent to its charging to 3.0 V. (g) Further high-magnification TEM image of AlPSe after it is discharged to 0.01 V. (h) HRTEM shots of AlPSe once it has been energized to 3.0 V. (i) Standard TEM appearance of AlPSe following its charge to the 3.0 V mark.

dendrite formation and stabilizing chalcogenides [77]. Overall, bimetallic compound electrodes offer enhanced structure, more active sites, and better conductivity in potassium-ion storage, leading to improved cycle life and capacity. Notably, after charging back to 3.0 V, an elemental ratio analysis performed with TEM reveals that the proportions of Ag, In, P, and Se are approximately 1:1:2:6, aligning with the mechanism of reverting back to AlPSe upon charging to 3.0 V, thus providing further supporting evidence.

Given the excellent cycling performance of AlPSe@G electrodes in lithium and potassium half-cells, we utilized AlPSe@G as an anode in a study aimed at assessing electrode material applicability and commercial potential [69,78,79]. We chose $LiFePO_4$ and Prussian Blue (PB) as cathode materials [80,81]. We used a 1 M $LiPF_6$ ECDECDMCFEC electrolyte in a lithium-ion full cell, maintaining an anode-to-cathode mass ratio of 1:5 for charge balance [82]. For potassium-ion cells, we synthesized Prussian Blue (PB) via coprecipitation (X-ray Diffraction patterns in Fig. S36) [83–86]. The potassium-ion cell used a 1 M KFSI DMC electrolyte with a 1:7 anode-to-cathode mass ratio. Fig. 8a shows a

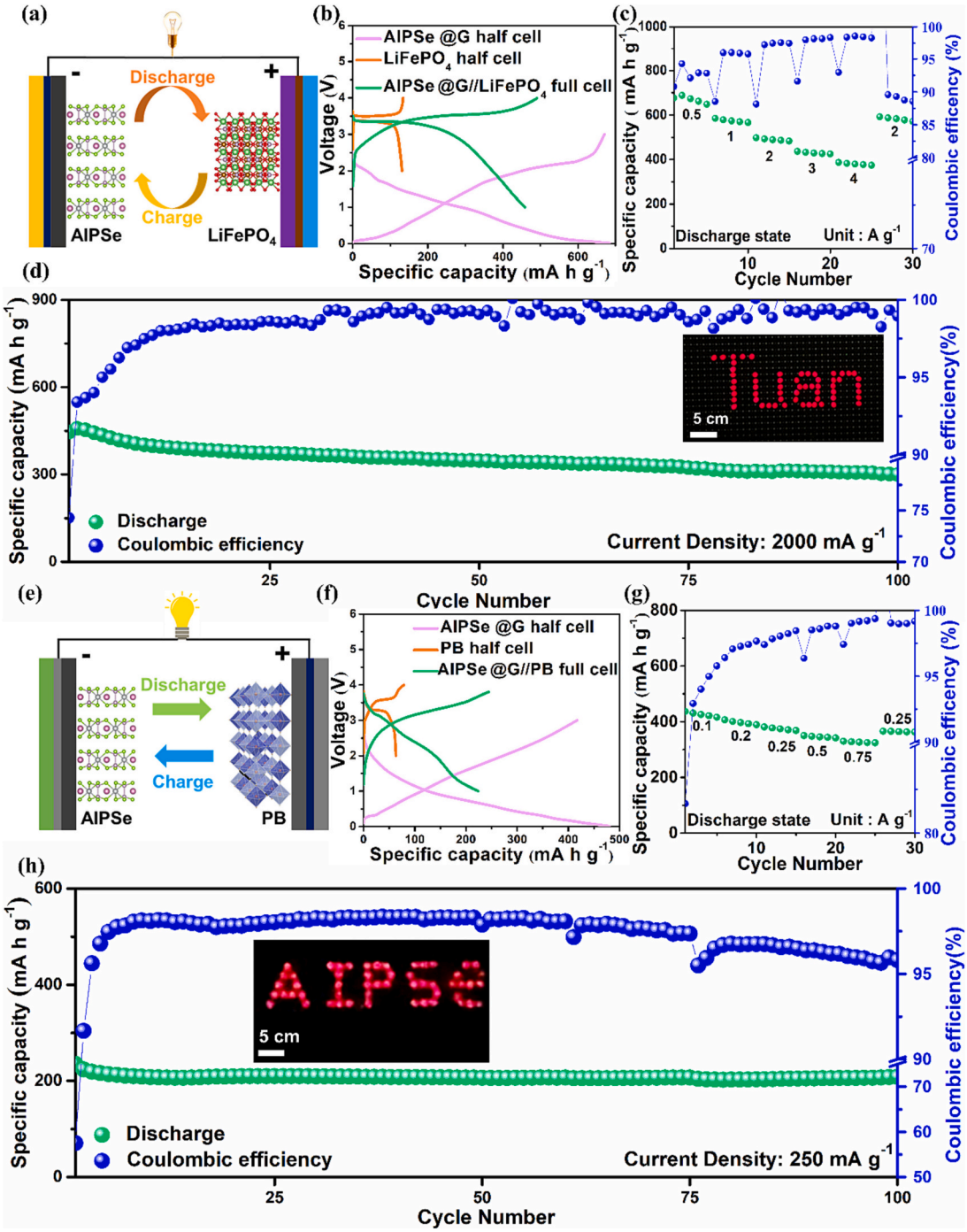

Fig. 8. (a) Illustrated model detailing the internal structure of a full cell comprising AlPSe@G and $LiFePO_4$ as active materials. (b) Voltage profiles during both discharge and charge cycles for individual $LiFePO_4$ and AlPSe@G half-cells, as well as a combined AlPSe@G//$LiFePO_4$ full cell. (c) Performance at different current rates observed for the AlPSe@G//$LiFePO_4$ full cell assembly. (d) Prolonged cycle life data for the AlPSe@G//$LiFePO_4$ lithium-ion full cell when operated at 2000 mA g^{-1}; a supplementary image within (d) showcases a lit LED bulb for illustrative purposes. (e) Conceptual blueprint of a full cell pairing AlPSe@G and PB. (f) Graphs depicting discharge and charge voltage variations for separate PB and AlPSe@G half-cells and a collective AlPSe@G//PB full cell. (g) Evaluation of the rate performance for the assembled AlPSe@G//PB full cell. (h) Extended cycling life analysis of the AlPSe@G//PB potassium-ion full cell at a current of 250 mA g^{-1}; an inset in (h) displays a lit LED bulb as a visual supplement.

schematic diagram illustrating the reaction of a LIB full cell, referred to as AlPSe@G//$LiFePO_4$, with AlPSe serving as the negative electrode, $LiFePO_4$ as the positive electrode. Fig. 8b shows the Galvanostatic Charge Discharge (GCD) curves of $LiFePO_4$ and AlPSe@G half cells and a AlPSe@G//$LiFePO_4$ full cell. Furthermore, the rate performance of AlPSe@G//$LiFePO_4$ was tested at various current densities of 0.5, 1.0, 2.0, 3.0, and 4.0 A g^{-1}, as shown in Fig. 8c. Fig. 8d reflects the long-term stability of the AlPSe@G//$LiFePO_4$ full cell, retaining 67.3 % capacity after 100 cycles at a current density of 2000 mA h g^{-1}, with an average Coulombic efficiency (CE) of 98.4 %. Meanwhile, the AlPSe@G//$LiFePO_4$ full cell also lighted up 59 red LED bulbs as shown in the inset of Fig. 8d. Fig. 8e shows a schematic diagram illustrating the reaction of a potassium-ion full cell, referred to as AlPSe@G//PB, with AlPSe serving as the negative electrode, PB as the positive electrode. Fig. 8f shows the

GCD curves of PB and AIPSe@G half cells and a AIPSe@G//PB full cell. The rate performance of AIPSe@G//PB was tested at various current densities of 0.1, 0.2, 0.25, 0.5, and 0.75 A g^{-1}, as shown in Fig. 8g, with corresponding discharge capacities of 408.5, 335.4, 318.3, 278.6, and 256.5 mA h g^{-1} based on the anode's mass. Fig. 8h represents the AIPSe@G//PB full cell's long-term stability, holding an 87.8 % capacity retention rate after 100 cycles at a current density of 250 mA h g^{-1} and an average CE of 97.1 %. Finally, the inset of Fig. 8h shows the AIPSe@G//PB full cell can lighted up 53 red LED bulbs.

3. Conclusion

In summary, we've developed anode electrodes for AMIBs by merging bimetallic MPTCs with 2D materials. Its superior electrochemical performance stems from the bimetallic synergy: silver mitigates volume expansion in LIBs, and indium serves as a buffer in PIBs, enhancing interface stability. In the discharge process of Lithium-ion batteries (LIBs), silver precipitates without reacting with Li^+. This behavior allows silver to act as a diluent, mitigating the extreme volumetric expansion, minimizing material fragmentation, and preventing the detachment of the active material from the current collector—factors that could otherwise contribute to a pronounced decrease in cycle life. In PIBs, the electrochemically inert component, indium (In), generated during discharge, serves to reinforce the structural stability of the material throughout the charging and discharging cycles. Moreover, simulation calculations reveal that the redox reactions of AIPSe are thermodynamically more favorable, emphasizing its probable proficiency as an anode in AMIBs. Using the bimetallization strategy, we've suppressed the problems associated dramatic volume expansion in 2D materials during charging and discharging, extending cycle life (LIBs: over 900 cycles, PIBs: over 550 cycles) and offer significant capacities (LIBs: 707.8 mA h g^{-1} (100 mA g^{-1}), PIBs: 480.3 mA h g^{-1} (25 mA g^{-1})). Successfully pairing with widely-used positive electrodes to build a full AMIB demonstrates its practical potential, offering a fresh option for the AMIB anode material system. This research emphasizes the advantages of bimetallization in 2D materials, and as such, bimetallized 2D materials emerge as strong candidates and offer valuable insights for the development of universal alkali metal ion anode materials.

4. Experimental section

4.1. Materials used

Raw materials include silver particles (sourced from UniRegion Bio-Tech, 99 % purity), indium particles (obtained from Alfa Aesar, with a 99.99 % purity), red phosphorus particulates (procured from Sigma-Aldrich, 97 % pure), and selenium particles (purchased from Alfa Aesar, 99.99 % pure). Additional chemicals like Sodium carboxymethyl cellulose, ethyl carbonate, diethyl carbonate, 1-Methyl-2-pyrrolidinone, and potassium metal were acquired from Sigma-Aldrich. KFSI was sourced from Combi-Blocks and DMC from NOVA material. Other reagents like LiPF6, FEC, graphite, LiFePO4, Super-P, and CR2032 coin cells were bought from Shining Energy. Glass fibers and copper foils were sourced from Advantec and Chang-Chun group, respectively. All substances were used as received, without further purification.

4.2. Material characterization

Material characterization was achieved through Scanning Electron Microscopy (SEM), X-ray Photoelectron Spectroscopy (XPS), Transmission Electron Microscopy (TEM), and X-ray Diffraction (XRD). SEM imaging was performed at an accelerating voltage of 10 kV and a working distance of 8 mm. TEM samples were readied by ethanol dispersion and deposited on copper and gold grids, followed by argon-atmosphere drying. XRD utilized Cu Kα radiation for analysis, and Raman spectra were obtained using a 532 nm excitation source.

4.3. Synthesis of AIPSe

Silver, indium, red phosphorus, and selenium particles, in a molar ratio of 1:1:2:6, were vacuum-sealed in a quartz tube. This tube was then subjected to a thermal treatment at 750 °C for one day. After cooling down to room temperature, the tube was carefully cut open, and samples were collected.

4.4. Synthesis of InSe

Indium and selenium powders, in a 1:1 M ratio, were sealed in a vacuum quartz tube. The tube was heated at 550 °C for 24 h. Once cooled, the tube was broken to retrieve the samples.

4.5. Synthesis of AIPSe@G

These composites were created using high-energy mechanical milling. AIPSe and InSe were mixed with graphite at a ratio of 3:1. The mixture was then ball milled for one full day.

4.6. Synthesis of Prussian blue (PB)

To produce Prussian Blue, two distinct solutions were prepared [87]. Solution A contained 5 millimoles of $FeCl_2{\cdot}4H_2O$ (sourced from Sigma Aldrich, 98 % pure) diluted in 50 mL of deionized water. Solution B was formulated by dissolving 5 millimoles of $K_4Fe(CN)_6{\cdot}3H_2O$ (from Sigma Aldrich, 99.5 % purity), 10 millimoles of potassium citrate, 200 millimoles of KCl (obtained from PubChem, 99 % pure), and 3 millimoles of ascorbic acid (from Sigma Aldrich, with purity exceeding 99 %) in 100 mL of deionized water. Carefully, Solution A was gradually mixed into Solution B. The resulting deep blue precipitate was separated by means of centrifugation, washed in triplicate with deionized water, and finally subjected to vacuum drying at a temperature of 100 °C for a duration of 16 h.

4.7. Electrochemical measurement

For the construction of the anode electrode, a uniform slurry was created by blending the active material AIPSe@G at a 3:1 ratio, Super P, and NaCMC in proportions of 7:2:1 using distilled water. This mixture was then spread onto copper foil with a doctor blade and subsequently air-dried at 80 °C in an environment of argon gas. The weight of the applied anode material approximated 0.8 to 1.0 mg per square centimeter. A Sartorius SE2 microbalance, accurate to 0.1 micrograms, was employed to gauge the mass of the electrode. Cyclic voltammetry data were gathered with a VMP3 multi-channel electrochemical analyzer from Bio-Logic Science Instruments. Assembling the coin-shaped half-cell, designated as CR2032, took place within an argon-saturated glovebox, utilizing custom-made potassium foil as a counter electrode. For LIBs, the half-cells were fitted with lithium foil as the counter electrode. The electrolyte fluid was a 1 M LiPF6 solution mixed in ethyl carbonate, dimethyl carbonate, and diethyl carbonate at equal volume percentages, along with a 10 % weight addition of fluoroethylene carbonate. In the case of PIBs, an electrolyte containing 1 M KFSI dissolved in DMC was introduced to saturate the anode electrode. A glass fiber separator and potassium foil were added in succession. Upon sealing the assembly, the battery's electrochemical attributes were put to the test using a Maccor Series 4000 battery tester. Evaluations took place across a voltage span ranging from 0.01 V to 3.0 V.

4.8. Computational section

Computational analysis using DFT was carried out through the VASP 5.4.4 software suite. Electron-ion interaction models utilized pseudopotentials based on the projector augmented wave method, in conjunction with the generalized gradient approximation (GGA-PBE)

functionals available in the VASP library. A plane-wave energy threshold was fixed at 400 eV. For the purpose of enhancing structural accuracy, the criteria for total energy and force convergence were established at $<1 \times 10^{-5}$ eV and below 0.03 eV/Å, respectively. When calculating transition states via the Climbing Image Nudged Elastic Band (CI-NEB) technique, the force convergence criteria were relaxed to <0.05 eV/Å to expedite convergence. To account for van der Waals interactions, Grimme's DFT-D3 approach was employed. Additionally, a vacuum layer of 15 Å thickness was introduced along the z-axis to nullify any undesired periodic effects.

CRediT authorship contribution statement

Yan-Jie Liao: Conceptualization, Methodology, Writing. Yi-Yen Hsieh: Data curation. Hsing-Yu Tuan: Conceptualization, Resources, Supervision, Writing - review & editing.

Declaration of competing interest

The authors declare that they have no known competing financial interests or personal relationships that could have appeared to influence the work reported in this paper.

Data availability

No data was used for the research described in the article.

Acknowledgments

This work received financial support from the 2030 Cross-Generation Young Scholars Program by Ministry of Science and Technology, Taiwan (NSTC 112-2628-E-007-010 & NSTC 112-2628-E-007-016). H.-Y. Tuan also acknowledges the financial support of National Tsing Hua University, Taiwan, through Grant No. 112B0011J2. The authors thank Ms. Y. M. Chang (Instrumentation center at NTHU) for spherical-aberration corrected field emission TEM analysis.

Appendix A. Supplementary data

Supplementary data to this article can be found online at https://doi.org/10.1016/j.est.2023.109737.

References

[1] B. Chen, D. Chao, E. Liu, M. Jaroniec, N. Zhao, S.Z. Qiao, Transition metal dichalcogenides for alkali metal ion batteries: engineering strategies at the atomic level, Energy Environ. Sci. 13 (4) (2020) 1096–1131, https://doi.org/10.1039/C9EE03549D.

[2] L. Zeng, L. Huang, J. Zhu, P. Li, P.K. Chu, J. Wang, X.F. Yu, Phosphorus-based materials for high-performance alkaline metal ion batteries: progress and prospect, Small 18 (39) (2022), 2201808, https://doi.org/10.1002/smll.202201808.

[3] C. Zhang, Q. Wang, Y. Song, G. Wang, H. Wang, 3D ordered hierarchically porous carbon derived from colloidal crystal templates towards alkali metal-ion batteries, Carbon 201 (2023) 76–99, https://doi.org/10.1016/j.carbon.2022.08.087.

[4] G. Liu, Z. Sun, X. Shi, X. Wang, L. Shao, Y. Liang, X. Lu, J. Liu, Z. Guo, 2D-layer-structure Bi to quasi-1D-structure $NiBi_3$: structural dimensionality reduction to superior sodium and potassium ion storage, Adv. Mater. (2023), 2305551, https://doi.org/10.1002/adma.202305551.

[5] D. Wang, C. Duan, Y. Yu, X. Li, Z. Wang, Y. Liu, C. Liu, Co-regulation of anion-cation in transition metal high entropy oxide for outstanding OER electrocatalytic performance, J. Alloys Compd. (2023), 171758, https://doi.org/10.1016/j.jallcom.2023.171758.

[6] J. Sun, Y. Xu, Y. Lv, Q. Zhang, X. Zhou, Recent advances in covalent organic framework electrode materials for alkali metal-ion batteries, CCS Chem. 5 (6) (2023) 1259–1276, https://doi.org/10.31635/ccschem.023.202302808.

[7] T. Yang, M. Fang, J. Liu, D. Yang, Y. Liang, J. Zhong, Y.J. Yuan, Y. Zhang, X. Liu, R. Zheng, Ultranarrow bandgap Se-deficient bimetallic selenides for high performance alkali metal-ion batteries, Adv. Funct. Mater. 32 (39) (2022), 2205880, https://doi.org/10.1002/adfm.202205880.

[8] S. Zhao, Z. Bian, Z. Liu, Y. Wang, F. Cui, H.G. Wang, G. Zhu, Bottom-up construction of fluorene-based porous aromatic frameworks for ultrahigh-capacity and high-rate alkali metal-ion batteries, Adv. Funct. Mater. 32 (44) (2022), 2204539, https://doi.org/10.1002/adfm.202204539.

[9] P. Wang, B. Xi, M. Huang, W. Chen, J. Feng, S. Xiong, Emerging catalysts to promote kinetics of lithium–sulfur batteries, Adv. Energy Mater. 11 (7) (2021), 2002893, https://doi.org/10.1002/aenm.202002893.

[10] Y. Dang, Z. Xu, H. Yang, K. Tian, Z. Wang, R. Zheng, H. Sun, Y. Liu, D. Wang, Designing water/air-stable Co-free high-entropy oxide cathodes with suppressed irreversible phase transition for sodium-ion batteries, Appl. Surf. Sci. 636 (2023), 157856, https://doi.org/10.1016/j.apsusc.2023.157856.

[11] G. Wang, M. Yu, X. Feng, Carbon materials for ion-intercalation involved rechargeable battery technologies, Chem. Soc. Rev. 50 (4) (2021) 2388–2443, https://doi.org/10.1039/D0CS00187B.

[12] X. Sun, Y. Chen, Y. Li, F. Luo, Biomass alginate derived oxygen-enriched carbonaceous materials with partially graphitic nanolayers for high performance anodes in lithium-ion batteries, Nanomaterials 13 (1) (2022) 82, https://doi.org/10.3390/nano13010082.

[13] W. Zhang, R. Huang, X. Yan, C. Tian, Y. Xiao, Z. Lin, L. Dai, Z. Guo, L. Chai, Carbon electrode materials for advanced potassium-ion storage, Angew. Chem. Int. Ed. (2023), e202308891, https://doi.org/10.1002/anie.202308891.

[14] W.C. Lin, Y.C. Yang, H.Y. Tuan, Ternary chalcogenide anodes for high-performance potassium-ion batteries and hybrid capacitors via composition-mediated bond softening and intermediate phase, Energy Stor. Mater. 51 (2022) 38–53, https://doi.org/10.1016/j.ensm.2022.06.010.

[15] T. Li, Y. Wang, Q. Zhou, L. Yuan, S. Qiao, M. Ma, Z. Liu, S. Chong, SnTe nanoparticles physicochemically encapsulated by double carbon as conversion-alloying anode materials for superior potassium-ion batteries, J. Mater. Sci. Technol. 158 (2023) 86–95, https://doi.org/10.1016/j.jmst.2023.02.027.

[16] K.T. Chen, S. Chong, L. Yuan, Y.C. Yang, H.Y. Tuan, Conversion-alloying dual mechanism anode: nitrogen-doped carbon-coated Bi_2Se_3 wrapped with graphene for superior potassium-ion storage, Energy Stor. Mater. 39 (2021) 239–249, https://doi.org/10.1016/j.ensm.2021.04.019.

[17] Y.F. Huang, Y.C. Yang, H.Y. Tuan, Construction of strongly coupled few-layer $FePSe_3$-CNT hybrids for high performance potassium-ion storage devices, Chem. Eng. J. 451 (2023), 139013, https://doi.org/10.1016/j.cej.2022.139013.

[18] Q. Zhou, L. Yuan, T. Li, S. Qiao, M. Ma, Y. Wang, S. Chong, Boosting cobalt ditelluride quantum-rods anode materials for excellent potassium-ion storage via hierarchical physicochemical encapsulation, J. Colloid Interface Sci. 646 (2023) 493–502, https://doi.org/10.1016/j.jcis.2023.05.073.

[19] L. Zhao, B. Ding, X.Y. Qin, Z. Wang, W. Lv, Y.B. He, Q.H. Yang, F. Kang, Revisiting the roles of natural graphite in ongoing lithium-ion batteries, Adv. Mater. 34 (18) (2022), 2106704, https://doi.org/10.1002/adma.202106704.

[20] L. Fan, R. Ma, Q. Zhang, X. Jia, B. Lu, Graphite anode for a potassium-ion battery with unprecedented performance, Angew. Chem. 131 (31) (2019) 10610–10615.

[21] F. Wu, C. Zhao, S. Chen, Y. Lu, Y. Hou, Y.S. Hu, J. Maier, Y. Yu, Multi-electron reaction materials for sodium-based batteries, Mater. Today 21 (9) (2018) 960–973, https://doi.org/10.1016/j.mattod.2018.03.004.

[22] J. Yang, Z. Ju, Y. Jiang, Z. Xing, B. Xi, J. Feng, S. Xiong, Enhanced capacity and rate capability of nitrogen/oxygen dual-doped hard carbon in capacitive potassium-ion storage, Adv. Mater. 30 (4) (2018), 1700104, https://doi.org/10.1002/adma.201700104.

[23] X. Yang, Y. Luo, J. Li, H. Wang, Y. Song, J. Li, Z. Guo, Tuning mixed electronic/ionic conductivity of 2D $CdPS_3$ nanosheets as an anode material by synergistic intercalation and vacancy engineering, Adv. Funct. Mater. 32 (18) (2022), 2112169, https://doi.org/10.1002/adfm.202112169.

[24] Y.F. Huang, Y.C. Yang, Y.Y. Tseng, H.Y. Tuan, Two dimensional $MnPSe_3$ layer stacking composites with superior storage performance for alkali metal-ion batteries, J. Colloid Interface Sci. 635 (2023) 336–347, https://doi.org/10.1016/j.jcis.2022.12.082.

[25] P.W. Chien, C.B. Chang, H.Y. Tuan, High-entropy two-dimensional metal phosphorus trichalcogenides boost high-performance potassium ion storage devices via electrochemical reconstruction, Energy Stor. Mater. (2023), 102853, https://doi.org/10.1016/j.ensm.2023.102853.

[26] C. Zhang, C. Lu, F. Zhang, F. Qiu, X. Zhuang, X. Feng, Two-dimensional organic cathode materials for alkali-metal-ion batteries, J. Energy Chem. 27 (1) (2018) 86–98, https://doi.org/10.1016/j.jechem.2017.11.008.

[27] K. Share, A.P. Cohn, R. Carter, B. Rogers, C.L. Pint, Role of nitrogen-doped graphene for improved high-capacity potassium ion battery anodes, ACS Nano 10 (10) (2016) 9738–9744, https://doi.org/10.1021/acsnano.6b05998.

[28] Z. Sun, H. Chang, Graphene and graphene-like two-dimensional materials in photodetection: mechanisms and methodology, ACS Nano 8 (5) (2014) 4133–4156, https://doi.org/10.1021/nn500508c.

[29] L. Peng, Y. Zhu, H. Li, G. Yu, Chemically integrated inorganic-graphene two-dimensional hybrid materials for flexible energy storage devices, Small 12 (45) (2016) 6183–6199, https://doi.org/10.1002/smll.201602109.

[30] J. Bao, L. Zhu, H. Wang, S. Han, Y. Jin, G. Zhao, Y. Zhu, X. Guo, J. Hou, H. Yin, Hexagonal boron nitride/blue phosphorene heterostructure as a promising anode material for Li/Na-ion batteries, J. Phys. Chem. C 122 (41) (2018) 23329–23335, https://doi.org/10.1021/acs.jpcc.8b07062.

[31] L. Liu, Z. Zhang, X. Liu, X. Xuan, B.I. Yakobson, M.C. Hersam, W. Guo, Borophene concentric superlattices via self-assembly of twin boundaries, Nano Lett. 20 (2) (2020) 1315–1321, https://doi.org/10.1021/acs.nanolett.9b04798.

[32] A.R. Jang, S. Hong, C. Hyun, S.I. Yoon, G. Kim, H.Y. Jeong, T.J. Shin, S.O. Park, K. Wong, S.K. Kwak, Wafer-scale and wrinkle-free epitaxial growth of single-orientated multilayer hexagonal boron nitride on sapphire, Nano Lett. 16 (5) (2016) 3360–3366, https://doi.org/10.1021/acs.nanolett.6b01051.

[33] M. Turiansky, A. Alkauskas, C. Van de Walle, Spinning up quantum defects in 2D materials, Nat. Mater. 19 (5) (2020) 487–489, https://doi.org/10.1038/s41563-020-0668-x.

[34] C. Rao, K. Gopalakrishnan, Borocarbonitrides, $B_xC_yN_z$: synthesis, characterization, and properties with potential applications, ACS Appl. Mater. Interfaces 9 (23) (2017) 19478–19494, https://doi.org/10.1021/acsami.6b08401.

[35] K.C. Lin, M.W. Lin, M.N. Hsu, G. Yu Chen, Y.C. Chao, H.Y. Tuan, C.S. Chiang, Y. C. Hu, Graphene oxide sensitizes cancer cells to chemotherapeutics by inducing early autophagy events, promoting nuclear trafficking and necrosis, Theranostics 8 (9) (2018) 2477. https://www.thno.org/v08p2477.htm.

[36] C. Yang, J. Feng, F. Lv, J. Zhou, C. Lin, K. Wang, Y. Zhang, Y. Yang, W. Wang, J. Li, Metallic graphene-like VSe_2 ultrathin nanosheets: superior potassium-ion storage and their working mechanism, Adv. Mater. 30 (27) (2018), 1800036, https://doi.org/10.1002/adma.201800036.

[37] B. Jia, Q. Yu, Y. Zhao, M. Qin, W. Wang, Z. Liu, C.Y. Lao, Y. Liu, H. Wu, Z. Zhang, Bamboo-like hollow tubes with MoS_2/N-doped-C interfaces boost potassium-ion storage, Adv. Funct. Mater. 28 (40) (2018), 1803409, https://doi.org/10.1002/adfm.201803409.

[38] L. Fang, J. Xu, S. Sun, B. Lin, Q. Guo, D. Luo, H. Xia, Few-layered tin sulfide nanosheets supported on reduced graphene oxide as a high-performance anode for potassium-ion batteries, Small 15 (10) (2019), 1804806, https://doi.org/10.1002/smll.201804806.

[39] L. Xing, K. Han, Q. Liu, Z. Liu, J. Chu, L. Zhang, X. Ma, Y. Bao, P. Li, W.A. Wang, Hierarchical two-atom-layered WSe_2/C ultrathin crumpled nanosheets assemblies: engineering the interlayer spacing boosts potassium-ion storage, Energy Stor. Mater. 36 (2021) 309–317, https://doi.org/10.1016/j.ensm.2021.01.005.

[40] H. Bretscher, Z. Li, J. Xiao, D.Y. Qiu, S. Refaely Abramson, J.A. Alexander Webber, A. Tanoh, Y. Fan, G. Delport, C.A. Williams, Rational passivation of sulfur vacancy defects in two-dimensional transition metal dichalcogenides, ACS Nano 15 (5) (2021) 8780–8789, https://doi.org/10.1021/acsnano.1c01220.

[41] S. Kang, S. Jeon, S. Kim, D. Seol, H. Yang, J. Lee, Y. Kim, Tunable out-of-plane piezoelectricity in thin-layered $MoTe_2$ by surface corrugation-mediated flexoelectricity, ACS Appl. Mater. Interfaces 10 (32) (2018) 27424–27431, https://doi.org/10.1021/acsami.8b06325.

[42] F. Liu, J. Zhou, C. Zhu, Z. Liu, Electric field effect in two-dimensional transition metal dichalcogenides, Adv. Funct. Mater. 27 (19) (2017), 1602404, https://doi.org/10.1002/adfm.201602404.

[43] H.J. Yang, C.Y. Chen, F.W. Yuan, H.Y. Tuan, Designed synthesis of solid and hollow $Cu_{2-x}Te$ nanocrystals with tunable near-infrared localized surface plasmon resonance, J. Phys. Chem. C 117 (42) (2013) 21955–21964, https://doi.org/10.1021/jp407559b.

[44] Y. Hao, A. Huang, S. Han, H. Huang, J. Song, X. Sun, Z. Wang, L. Li, F. Hu, J. Xue, Plasma-treated ultrathin ternary $FePSe_3$ nanosheets as a bifunctional electrocatalyst for efficient zinc–air batteries, ACS Appl. Mater. Interfaces 12 (26) (2020) 29393–29403, https://doi.org/10.1021/acsami.0c08133.

[45] X. Hou, X. Zhang, Q. Ma, X. Tang, Q. Hao, Y. Cheng, T. Qiu, Alloy engineering in few-layer manganese phosphorus trichalcogenides for surface-enhanced raman scattering, Adv. Funct. Mater. 30 (12) (2020), 1910171, https://doi.org/10.1002/adfm.201910171.

[46] H. Li, N. Wells, B. Chong, B. Xu, J. Wei, B. Yang, G. Yang, The layered cadmium phosphorus trichalcogenides nanosheet with anion mono-doping: a new candidate for solar-driven water splitting, Chem. Eng. Sci. 229 (2021), 116069, https://doi.org/10.1016/j.ces.2020.116069.

[47] S. Thinius, M.M. Islam, P. Heitjans, T. Bredow, Theoretical study of Li migration in lithium–graphite intercalation compounds with dispersion-corrected DFT methods, J. Phys. Chem. C 118 (5) (2014) 2273–2280, https://doi.org/10.1021/jp408945j.

[48] X. Xie, T. Makaryan, M. Zhao, K.L. Van Aken, Y. Gogotsi, G. Wang, MoS_2 nanosheets vertically aligned on carbon paper: a freestanding electrode for highly reversible sodium-ion batteries, Adv. Energy Mater. 6 (5) (2016), 1502161, https://doi.org/10.1002/aenm.201502161.

[49] J. Zhou, L. Wang, M. Yang, J. Wu, F. Chen, W. Huang, N. Han, H. Ye, F. Zhao, Y. Li, Hierarchical VS_2 nanosheet assemblies: a universal host material for the reversible storage of alkali metal ions, Adv. Mater. 29 (35) (2017), 1702061, https://doi.org/10.1002/adma.201702061.

[50] J. Yang, X. Xiao, W. Gong, L. Zhao, G. Li, K. Jiang, R. Ma, M.H. Rummeli, F. Li, T. Sasaki, Size-independent fast ion intercalation in two-dimensional titania nanosheets for alkali-metal-ion batteries, Angew. Chem. Int. Ed. 131 (26) (2019) 8832–8837, https://doi.org/10.1002/ange.201902478.

[51] X. Xie, M. Mao, S. Qi, J. Ma, ReS_2-based electrode materials for alkali-metal ion batteries, CrystEngComm 21 (25) (2019) 3755–3769, https://doi.org/10.1039/C9CE00531E.

[52] L. Hou, L. Zhang, J. Zang, W. Shen, T. Zhang, X. Huang, H. Yuan, D. Kong, Y. Wang, X. Li, Rational design of Fe-doped $K_{0.8}Ti_{1.73}Li_{0.27}O_4$@rGO as a high-rate and long-cycle-life anode for lithium-ion batteries, J. Phys. D 55 (23) (2022), 234002, https://doi.org/10.1088/1361-6463/ac5144.

[53] S. Haghighat Shishavan, M. Nazarian Samani, M. Nazarian Samani, S.H. Hosseini Shokouh, T. Maschmeyer, K.B. Kim, Realization of $Sn_2P_2S_6$-carbon nanotube anode with high K^+/Na^+ storage performance via rational interface manipulation–induced shuttle-effect inhibition and self-healing, Chem. Eng. J. 435 (2022), 134965, https://doi.org/10.1016/j.cej.2022.134965.

[54] K.Z. Du, X.Z. Wang, Y. Liu, P. Hu, M.I.B. Utama, C.K. Gan, Q. Xiong, C. Kloc, Weak Van der Waals stacking, wide-range band gap, and raman study on ultrathin layers of metal phosphorus trichalcogenides, ACS Nano 10 (2) (2016) 1738–1743, https://doi.org/10.1021/acsnano.5b05927.

[55] G. Fang, Z. Wu, J. Zhou, C. Zhu, X. Cao, T. Lin, Y. Chen, C. Wang, A. Pan, S. Liang, Observation of pseudocapacitive effect and fast ion diffusion in bimetallic sulfides as an advanced sodium-ion battery anode, Adv. Energy Mater. 8 (19) (2018), 1703155, https://doi.org/10.1002/aenm.201703155.

[56] X. Wang, Z. Li, Y. Qu, T. Yuan, W. Wang, Y. Wu, Y. Li, Review of metal catalysts for oxygen reduction reaction: from nanoscale engineering to atomic design, Chem 5 (6) (2019) 1486–1511, https://doi.org/10.1016/j.chempr.2019.03.002.

[57] H.Y. Zhong, X. Lu, Y. Zhong, Y. Zhao, X.M. Liu, D.H. Cheng, X.Y. Huang, K.Z. Du, X. H. Wu, Lithium storage performance boosted via delocalizing charge in $Zn_xCo_{1-x}PS_3/CoS_2$ of 2D/3D heterostructure, Small 18 (2) (2022), 2104295, https://doi.org/10.1002/smll.202104295.

[58] Y.J. Liao, W.W. Shen, C.B. Chang, H.Y. Tuan, High-entropy transition metal disulfide colloid clusters: synergistic atomic scale interaction and interconnected network for ultra-stable potassium ion storage, Chem. Eng. J. (2023), 143942, https://doi.org/10.1016/j.cej.2023.143942.

[59] C.G. Zhang, W.X. Ji, P. Li, C.W. Zhang, P.J. Wang, Tuning the electronic and optical properties of two-dimensional $AgBiP_2Se_6$ and $AgInP_2Se_6$ Janus monolayers, Chem. Phys. Lett. 780 (2021), 138933, https://doi.org/10.1016/j.cplett.2021.138933.

[60] S.F. Ho, Y.C. Yang, H.Y. Tuan, Silver boosts ultra-long cycle life for metal sulfide lithium-ion battery anodes: taking $AgSbS_2$ nanowires as an example, J. Colloid Interface Sci. 621 (2022) 416–430, https://doi.org/10.1016/j.jcis.2022.04.020.

[61] S. Lei, M. Qiu, X. Hu, L.M. Sheng, J. Li, Y. Liu, J. Yuan, H. Zhan, Z. Wen, Heteroatomic phosphorus selenides molecules encapsulated in porous carbon as a highly reversible anode for sodium-ion batteries, Mater. Today Nano 22 (2023), 100344, https://doi.org/10.1016/j.mtnano.2023.100344.

[62] M. Xiao, Y. Miao, Y. Tian, Y. Yan, Synthesizing nanoparticles of Co-P-Se compounds as electrocatalysts for the hydrogen evolution reaction, Electrochim. Acta 165 (2015) 206–210, https://doi.org/10.1016/j.electacta.2015.03.023.

[63] Y. Wu, Z. Wang, Z. Wang, X. Liu, S. Zhang, C. Deng, Tailoring stress-relieved structure for ternary cobalt phosphoselenide@ N/P codoped carbon towards high-performance potassium-ion hybrid capacitors and potassium-ion batteries, Energy Stor. Mater. 57 (2023) 180–194.

[64] X. Shen, H. Sun, B. Li, Y. Yuan, L. Zhang, S. Li, L. Wang, B. Lu, J. Zhu, X. Duan, Dual-strategy coupling driven versatile carbon-based anode for potassium-ion/potassium metal storage, Chem. Eng. J. 473 (2023), 145155, https://doi.org/10.1016/j.cej.2023.145155.

[65] H. Yang, F. He, F. Liu, Z. Sun, Y. Shao, L. He, Q. Zhang, Y. Yu, Simultaneous catalytic acceleration of white phosphorus polymerization and red phosphorus potassiation for high-performance potassium-ion batteries, Adv. Mater. n/a(n/a) 2306512. doi:https://doi.org/10.1002/adma.202306512.

[66] H. Jin, H. Wang, Z. Qi, D.-S. Bin, T. Zhang, Y. Wan, J. Chen, C. Chuang, Y.-R. Lu, T.-S. Chan, H. Ju, A.-M. Cao, W. Yan, X. Wu, H. Ji, L.-J. Wan, A black phosphorus–graphite composite anode for Li-/Na-/K-ion batteries, Angew. Chem. Int. Ed. 59 (6) (2020) 2318–2322, https://doi.org/10.1002/anie.201913129.

[67] Y.Y. Hsieh, H.Y. Tuan, Architectural van der Waals Bi_2S_3/Bi_2Se_3 topological heterostructure as a superior potassium-ion storage material, Energy Stor. Mater. 51 (2022) 789–805, https://doi.org/10.1016/j.ensm.2022.07.020.

[68] W.W. Shen, Y.Y. Hsieh, H.Y. Tuan, 3D space-confined $Co_{0.85}Se$ architecture with effective interfacial stress relaxation as anode material reveals robust and highly loading potassium-ion batteries, J. Colloid Interface Sci. 643 (2023) 626–639, https://doi.org/10.1016/j.jcis.2023.04.018.

[69] X. Yi, A.M. Rao, J. Zhou, B. Lu, Trimming the degrees of freedom via a K^+ flux rectifier for safe and long-life potassium-ion batteries, Nano-Micro Lett. 15 (1) (2023) 200, https://doi.org/10.1007/s40820-023-01178-3.

[70] X. Yi, Y. Feng, A.M. Rao, J. Zhou, C. Wang, B. Lu, Quasi-solid aqueous electrolytes for low-cost sustainable alkali-metal batteries, Adv. Mater. 35 (29) (2023), 2302280, https://doi.org/10.1002/adma.202302280.

[71] G. Zhang, X. Li, D. Wei, H. Yu, J. Ye, S. Chen, W. Zhang, J. Zhu, X. Duan, Synergistic engineering of structural and electronic regulation of In2Se3 for ultrastable Li − ion battery, Chem. Eng. J. 453 (2023), https://doi.org/10.1016/j.cej.2022.139841.

[72] Q. He, B. Yu, Z. Li, Y. Zhao, Density functional theory for battery materials, EEM 2 (4) (2019) 264–279, https://doi.org/10.1002/eem2.12056.

[73] C.J. Zhang, M. Liang, S.H. Park, Z. Lin, A. Seral Ascaso, L. Wang, A. Pakdel, C. O. Coileain, J. Boland, O. Ronan, Extra lithium-ion storage capacity enabled by liquid-phase exfoliated indium selenide nanosheets conductive network, Energy Environ. Sci. 13 (7) (2020) 2124–2133, https://doi.org/10.1039/D0EE01052A.

[74] S. Wang, T. Cui, L. Shao, S. Yang, L. Yu, J. Guan, X. Shi, J. Cai, Z. Sun, In-situ fabrication of active interfaces towards FeSe as advanced performance anode for sodium-ion batteries, J. Colloid Interface Sci. 627 (2022) 922–930.

[75] J.Z. Yen, C.B. Chang, K.S. Jhang, H.Y. Tuan, Excellent metal phosphide electrode for potassium ion hybrid capacitors: the case of carbon nanotube-wrapped AgP_2, ACS Appl. Energy Mater. 6 (2) (2023) 822–831, https://doi.org/10.1021/acsaem.2c03113.

[76] Y. Huang, Z. Wang, Y. Jiang, S. Li, M. Wang, Y. Ye, F. Wu, M. Xie, L. Li, R. Chen, Conductivity and pseudocapacitance optimization of bimetallic antimony–indium sulfide anodes for sodium-ion batteries with favorable kinetics, Adv. Sci. 5 (10) (2018), 1800613, https://doi.org/10.1002/advs.201800613.

[77] S. Luo, Z. Wang, X. Li, X. Liu, H. Wang, W. Ma, L. Zhang, L. Zhu, X. Zhang, Growth of lithium-indium dendrites in all-solid-state lithium-based batteries with sulfide electrolytes, Nat. Commun. 12 (1) (2021) 6968, https://doi.org/10.1038/s41467-021-27311-7.

[78] Y.Y. Hsieh, K.T. Chen, H.Y. Tuan, A synergetic SnSb-amorphous carbon composites prepared from polyesterification process as an ultrastable potassium-ion battery anode, Chem. Eng. J. 420 (2021), 130451, https://doi.org/10.1016/j.cej.2021.130451.

[79] T. Wang, Y. Tang, M. Yu, B. Lu, X. Zhang, J. Zhou, Spirally grown zinc-cobalt alloy layer enables highly reversible zinc metal anodes, Adv. Funct. Mater. (2023), 2306101, https://doi.org/10.1002/adfm.202306101.
[80] C.H. Chang, K.T. Chen, Y.Y. Hsieh, C.B. Chang, H.Y. Tuan, Crystal facet and architecture engineering of metal oxide nanonetwork anodes for high-performance potassium ion batteries and hybrid capacitors, ACS Nano 16 (1) (2022) 1486–1501, https://doi.org/10.1021/acsnano.1c09863.
[81] J. Shim, K.A. Striebel, Cycling performance of low-cost lithium ion batteries with natural graphite and $LiFePO_4$, J. Power Sources 119 (2003) 955–958, https://doi.org/10.1016/S0378-7753(03)00297-0.
[82] X. Kong, X. Zhao, C. Li, Z. Jia, C. Yang, Z. Wu, X. Zhao, Y. Zhao, F. He, Y. Ren, Terminal group-oriented self-assembly to controllably synthesize a layer-by-layer $SnSe_2$ and MXene heterostructure for ultrastable lithium storage, Small 19 (14) (2023), 2206563, https://doi.org/10.1002/smll.202206563.
[83] A. Zhou, W. Cheng, W. Wang, Q. Zhao, J. Xie, W. Zhang, H. Gao, L. Xue, J. Li, Hexacyanoferrate-type prussian blue analogs: principles and advances toward high-performance sodium and potassium ion batteries, Adv. Energy Mater. 11 (2) (2021), 2000943, https://doi.org/10.1002/aenm.202000943.
[84] Z. Wang, W. Zhuo, J. Li, L. Ma, S. Tan, G. Zhang, H. Yin, W. Qin, H. Wang, L. Pan, Regulation of ferric iron vacancy for Prussian blue analogue cathode to realize high-performance potassium ion storage, Nano Energy 98 (2022), 107243, https://doi.org/10.1016/j.nanoen.2022.107243.
[85] T. Hosaka, T. Fukabori, H. Kojima, K. Kubota, S. Komaba, Effect of particle size and anion vacancy on electrochemical potassium ion insertion into potassium manganese hexacyanoferrates, ChemSusChem 14 (4) (2021) 1166–1175, https://doi.org/10.1002/cssc.202002628.
[86] L. Li, Z. Hu, Y. Lu, C. Wang, Q. Zhang, S. Zhao, J. Peng, K. Zhang, S.L. Chou, J. Chen, A low-strain potassium-rich prussian blue analogue cathode for high power potassium-ion batteries, Angew. Chem. Int. Ed. 133 (23) (2021) 13160–13166, https://doi.org/10.1002/ange.202103475.
[87] C. Zhang, Y. Xu, M. Zhou, L. Liang, H. Dong, M. Wu, Y. Yang, Y. Lei, Potassium Prussian blue nanoparticles: a low-cost cathode material for potassium-ion batteries, Adv. Funct. Mater. 27 (4) (2017), 1604307, https://doi.org/10.1002/adfm.201604307.